International Journal of Naval Architecture and Ocean Engineering 18 (2026) 100766

Contents lists available at ScienceDirect

International Journal of Naval Architecture and Ocean Engineering

journal homepage: www.journals.elsevier.com/international-journal-of-naval-architecture-and-ocean-engineering/

Optimising geometries of drag embedment anchors for floating offshore structures using a multi-objective evolutionary algorithm

D.A. Dao [a],*, A. Chmelnizkij [b], K. Cerek [a], E. Hadjiloo [a], J. Grabe [a], K. Smarsly [b]

[a] Institute of Geotechnical Engineering and Construction Management, Hamburg University of Technology, Hamburg, Germany
[b] Institute of Digital and Autonomous Construction, Hamburg University of Technology, Blohmstraße 15, Hamburg, Germany

ARTICLE INFO

Keywords:
Drag embedment anchors (DEAs)
Optimisation
Multi-objective evolutionary algorithm
Offshore renewables
Floating structures

ABSTRACT

Floating offshore renewable energy systems rely on secure anchoring, e.g. drag embedment anchors (DEAs). DEA design involves balancing multiple objectives and considering various geometric parameters. Although multi-objective optimisation packages are widely available, DEA optimisation is still frequently handled heuristically. This study introduces a workflow that couples established semi-analytical DEA kinematics in MATLAB with multi-objective evolutionary optimisation (gamultiobj, based on NSGA-II) to identify anchor geometries that minimise anchor volume while maximising bearing capacity and penetration depth. Radar charts and the visualisation of the Pareto front across the design space provide interpretable structures that are not directly apparent from the governing equations alone. Three case studies are presented. The first identifies Pareto-optimal fluke and shank lengths and examines the influence of the boundary on the solutions. The second expands the design space to include fluke thickness, junction length, and fluke–shank angle. Clustering of Pareto solutions reveals three consistent geometric groups: (i) generally large anchors with small junctions, (ii) anchors with larger junctions and variable proportions, and (iii) anchors with broad flukes. A high fluke-shank angle is consistently present across all groups and appears beneficial for all objectives. The third case applies a weighted-sum formulation to produce a single design. Overall, this study provides a workflow for optimisation-driven exploration of DEA design, including a classification of Pareto-optimal geometries that offers a compact way to assess trade-offs from concept to sizing.

1. Introduction

1.1. Drag embedment anchors

Drag embedment anchors (DEAs) are widely used for station-keeping of temporary and permanent floating structures, including ships, oil and gas platforms, and floating offshore wind turbines (FOWTs) (Cerfontaine et al., 2023), as presented in Fig. 1. In particular, FOWTs represent a key technology in the transition to renewable energy, which increases the demand for reliable and efficient anchor design under both installation loads and new loading conditions induced by turbine operation (Putuhena et al., 2023; Gourvenec, 2024).

Anchor optimisation has traditionally relied on heuristic approaches and remains an active field of research. In addition to ongoing empirical and analytical developments, numerical and experimental methods are increasingly used to quantify the behaviour of DEAs with greater precision, as shown in Fig. 2 (Delmar, 2018; Shin et al., 2011; Sharif et al., 2025; Dao et al., 2025a; Lai et al., 2025a; Fan et al., 2026; Wu et al., 2026).

Semi-analytical models presented by Neubecker and Randolph (1996), Thorne (1998), and Dahlberg (1998) predict the anchor trajectory and bearing capacity of DEAs in clay using limit equilibrium analysis. International standards, including the ABS (2018), have incorporated subsequent enhancements by Aubeny and Chi (2010), Aubeny et al. (2011) which form the basis for this study. Numerical investigations of the anchor installation process using large deformation finite element simulations have extended the DEA analysis into three dimensions (Dou and Yu, 2018; Dao et al., 2023; Dao and Dicke, 2024).

Both numerical and semi-analytical solutions highlight dependencies on various parameters related to anchor geometry and seabed conditions, which complicates the derivation of a single optimal design. An effective DEA configuration must balance multiple performance criteria rather than optimising a single objective, emphasising the need for multi-objective optimisation. In the following, a possible multi-objective optimisation approach for DEA geometry is presented, providing a workflow for exploration and classification of Pareto-optimal designs.

---

* Corresponding author.
E-mail address: duy.anh.dao@tuhh.de (D.A. Dao).

https://doi.org/10.1016/j.ijnaoe.2026.100766
Received 21 January 2026; Received in revised form 13 April 2026; Accepted 13 April 2026

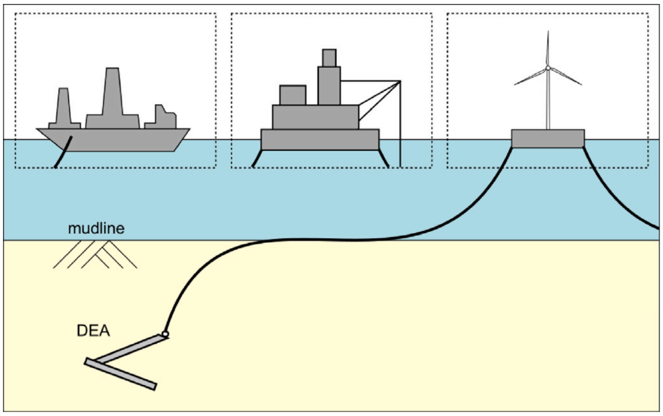

Fig. 1. DEA-secured floating structures.

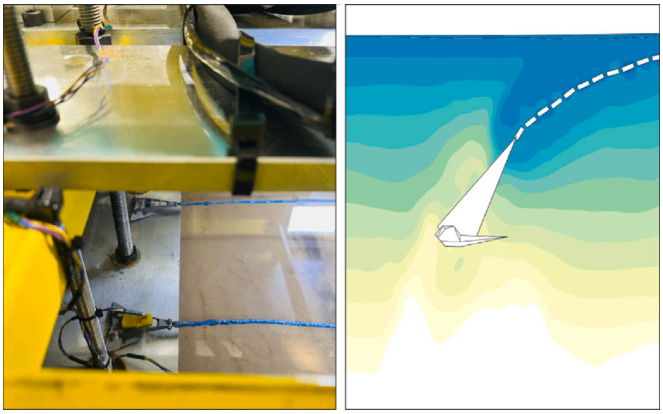

Fig. 2. Left: Centrifuge setup for DEA behaviour testing. Right: Contour plot of vertical stress distribution obtained from numerical simulations with CEL.

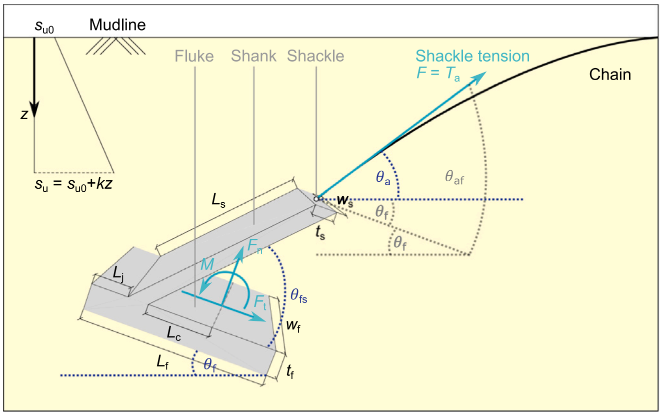

Fig. 3. DEA model applied in this study.

1.2. Multi-objective evolutionary optimisation in geotechnical engineering

Multi-objective evolutionary algorithms are suitable for DEA optimisation as they efficiently handle conflicting design objectives. As Pareto-based approaches, multi-objective evolutionary algorithms identify a diverse set of Pareto-optimal solutions, enabling a comprehensive trade-off between various objectives. The trade-off ensures robust design selection based on project-specific constraints such as cost, material availability, or seabed conditions. Additionally, these algorithms are able to handle nonlinearities and constraints inherent in DEA behaviour.

With adequate convergence and comparable parameter settings, similar Pareto fronts across established multi-objective evolutionary algorithms (e.g., non-dominated sorting genetic algorithm NSGA-II, gamultiobj, or SPEA) and many-objective evolutionary algorithms (e.g., NSGA-III) are to be expected. In this study, therefore, the gamultiobj (based on NSGA-II) in MATLAB is used and briefly summarised in the following.

NSGA-II has been widely applied in material parameter calibration, structure-soil interaction (SSI), topology optimisation, and foundation design. In material parameter calibration, NSGA-II has been employed to optimise constitutive model parameters and discrete element method (DEM) models, improving soil behaviour predictions (Gras et al., 2017; An et al., 2025; He et al., 2024; Zhong et al., 2019). In SSI problems, NSGA-II has enhanced the design of tuned mass dampers, bridge-embankment transitions, soil reinforcements, and pile foundations, considering soil stiffness and dynamic response (Khoshnoudian et al., 2016; Shan et al., 2022; Gong et al., 2013; Li et al., 2022; Deb and Dhar, 2010; Zhou et al., 2023; Amanat et al., 2023). Cerek and Grabe (2022), Cerek et al. (2024) applied NSGA-II to optimise dike geometry for stability, including sustainability objectives such as CO_2 emissions and material efficiency.

The gamultiobj function in MATLAB is a variant of the conventional NSGA-II algorithm by Deb et al. (2002a) regarding selection, diversity preservation, and genetic operators (MathWorks, 2025b). The gamultiobj algorithm is well-suited for DEA design because it can handle the multiple interdependent parameters and objective functions required by the process. The selection mechanism of the algorithm ensures a reliable search for global minima, making the algorithm an effective tool for geotechnical design applications that require balancing multiple performance criteria (MathWorks, 2025a,c).

1.3. Objectives and structure

This study aims to present a workflow for optimisation-driven exploration of DEA design and to identify patterns in Pareto-optimal geometries under the governing DEA equations. To this end, this work determines, which geometrical configurations of L_f, L_s, θ_{fs}, t_s and L_j (Fig. 3) offer the most practical and efficient solutions based on existing semi-analytical approaches for DEA performance. Finding these solutions is essential for designing sustainable and safe offshore infrastructure. Therefore, this study employs a multi-objective framework to evaluate DEA designs, focusing on trade-offs between the following three objectives, including:

- **Minimising volume** of the anchor to reduce its mass, which eases the handling during installation and retrieval. A smaller volume also contributes to lower material costs, making the anchor more economically feasible.
- **Maximising resistance** of the anchor ensures greater holding power for the stability and safety of the anchored structure.
- **Maximising embedment depth** provides additional security against pull-out due to external factors such as ship anchors and fishing equipment.

The three objectives represent efficiency, safety and cost-effectiveness of the anchors.

Following the introduction, the model for DEA analysis is described in Section 2. Section 3 outlines the optimisation algorithm applied in this study. Section 4 presents three case studies in which the optimisation is used to identify Pareto-optimal anchor geometries. In the first case study, the optimisation is performed with two geometric parameters, i.e. fluke length L_f and shaft length L_s. The second case study extends the parameter set by including three additional decision variables. Both studies yield a set of Pareto-optimal solutions represented by a Pareto front. In the third case study, a weighted sum of

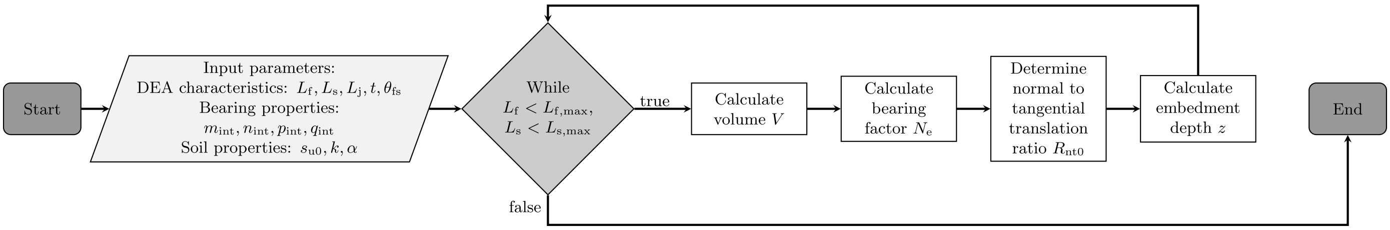

Fig. 4. Process for the DEA analysis conducted by the MATLAB code: Computation of the anchor volume V, the bearing capacity factor N_e and the embedment depth z throughout the drag distance while varying the fluke L_f and shank L_s lengths with the remaining input parameters staying constant.

Table 1
Input parameters for DEA analysis based on ^{A}Delmar (2018), ^{B}Aubeny and Chi (2010) and ^{C}Murff et al. (2005).

Parameter	Value	Unit	Definition	Source
L_f	2.9 to 4.0	m	Fluke length	A,B
L_s	4 to 8	m	Shank length	A,B
t_f	$0.14L_f$	m	Fluke thickness	A,B
t_s	t_f	m	Shank thickness	A,B
w_f	L_f	m	Fluke width	A,B
w_s	w_f	m	Shank width	A,B
L_j	$0.25L_f$	m	Junction length	A,B
θ_{fs}	50	°	Fluke–shank angle	A,B
S_t	3	–	Sensitivity	B
α	$1/S_t$	–	Adhesion coefficient	B,C
m_{int}	1.56	–	Interaction coefficient	B,C
n_{int}	4.19	–	Interaction coefficient	B,C
p_{int}	1.57	–	Interaction coefficient	B,C
q_{int}	4.43	–	Interaction coefficient	B,C
b_{chain}	0.1	m	Line diameter	A,B
N_{chain}	12	–	Bearing factor	B
E_n	1	–	Multiplier	B
s_{u0}	2	kPa	Mudline strength	B
k	1.60	kPa/m	Strength gradient	B
dt	1	–	Distance step	–
$\theta_{a,0}$	1	°	Anchor line angle	–
$\theta_{f,0}$	$\theta_{af0} - \theta_{a,0}$	°	Fluke angle	–

the objectives is applied to identify a single preferred solution from the Pareto front. Finally, Section 5 provides conclusions and an outlook on future work.

2. Governing equations for DEA analysis

This section presents the governing equations that describe the anchor volume, bearing capacity, and embedment depth. The equations are based on a DEA which is subjected to a combination of normal and tangential loading (F_n and F_t), and a moment (M), according to Fig. 3. The presented analysis is based on relationships originally proposed by Murff (1994) for shallow foundations, which was later adopted and further developed by O'Neill et al. (2003) and Aubeny and Chi (2010). The latter approach serves as the basis for the MATLAB code used in the DEA analysis, as detailed by Dao et al. (2024b), with its general computational process presented in Fig. 4. The code is available at Chmelnizkij and Dao (2025). Table 1 lists all input values which include anchor geometries, soil conditions and interaction properties.

Anchor volume V

The volume V directly correlates with the amount of material needed to manufacture a particular anchor design. The volume for the simplified DEA is calculated using Eq. (1):

$$V = (L_f + \sin(\theta_{fs})L_s)t_f w_f. \tag{1}$$

Fig. 5 shows the optimum for the volume S1 for $L_f = 2.9$ m and $L_s = 4$ m for the given input values.

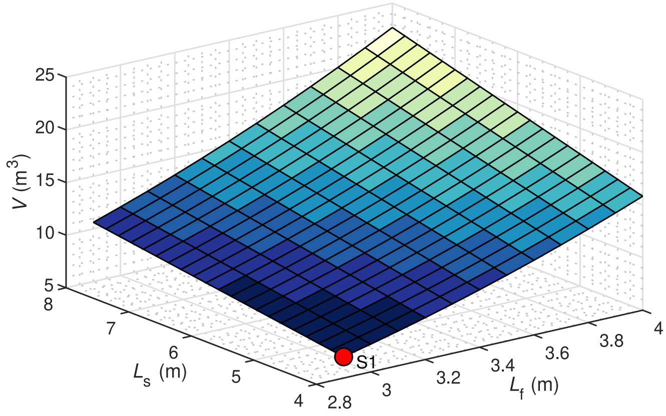

Fig. 5. Volume V as a function of fluke length L_f and shank length L_s, including the single-objective volume-optimal solution (S1).

Bearing capacity factor N_e

To obtain N_e, the combination of normal and tangential forces F_n and F_t, and the moment M acting at the centre of the fluke at $L_c = L_f - (L_j + t_s)/2$, as shown in Fig. 3, must be evaluated. The interaction of these loads is described through the function f in Eq. (2), as initially introduced by Murff (1994) for strip and rectangular plates and later applied to drag anchors by O'Neill et al. (2003), as well as Aubeny and Chi (2010). To find the bearing capacity factor N_e, Eq. (2) needs to equal 0:

$$f = \left(\frac{|c_1| \cdot N_e}{N_{n,max}}\right)^{q_{int}} + \left(\left(\frac{|c_3| \cdot N_e}{N_{m,max}}\right)^{m_{int}} + \left(\frac{|c_2| \cdot N_e}{N_{t,max}}\right)^{n_{int}}\right)^{\frac{1}{p_{int}}} - 1. \tag{2}$$

A detailed description of the parameters used in Eq. (2) is provided by Dao et al. (2024b,a) and Cerek et al. (2025). Fig. 6 shows the bearing factor N_e under varying loading angles θ_{af}, across a spectrum of fluke and shank lengths L_f and L_s. A critical loading scenario arises when the moment is cancelled, occurring when the line of action intersects the central point of the anchor. Under these conditions, the bearing factor N_e aligns with the rotational-neutral bearing factor N_{e0}, which corresponds to the bearing factor N_{et} (red curve) observed during pure tangential loading. In instances where these factors do not intersect, the code adopts the adjacent point, defined as the value of θ_{af} that minimises the difference between N_{et} and N_e. In cases where these points intersect multiple times, the algorithm uses the initial intersection point to determine N_{e0} and ultimately obtains N_{e0}. Fig. 7 shows the maximum bearing factor $N_{e,max}$ varying with the fluke and shank lengths, with its optimum S2 for $L_f = L_s = 4$ m.

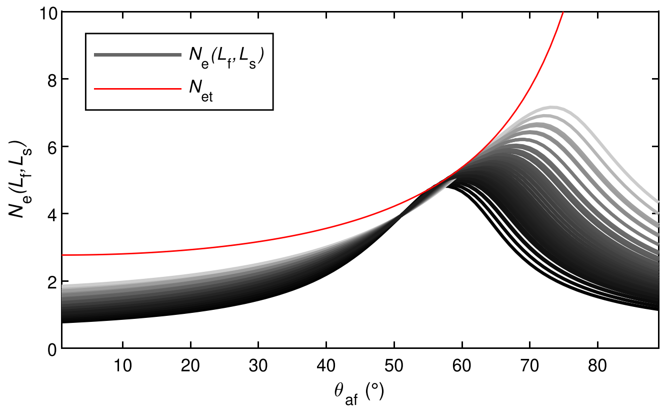

Fig. 6. Bearing factor $N_\mathrm{e}(L_\mathrm{f}, L_\mathrm{s})$ over θ_af and the bearing capacity factor with only tangential loading N_et.

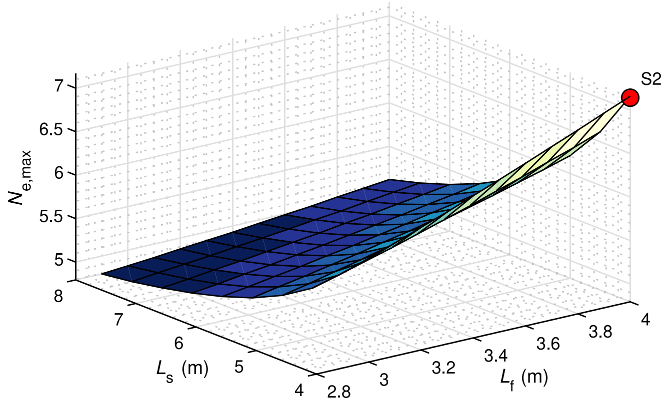

Fig. 7. Maximum bearing factor $N_\mathrm{e,max}$ as a function of fluke length L_f and shank length L_s, including the single-objective bearing factor-optimal solution (S2).

Embedment depth z

Fig. 8 presents the MATLAB code flow for the embedment analysis. The ratio of normal to tangential translation R_nt0 is given by Eq. (3):

$$R_\mathrm{nt0} = \frac{\frac{N_\mathrm{t,max}}{N_\mathrm{n,max}} \frac{p_\mathrm{int} q_\mathrm{int}}{n_\mathrm{int}}}{\left(\left| \frac{N_\mathrm{e0} c_3}{N_\mathrm{m,max}} \right|^{m_\mathrm{int}} + \left| \frac{N_\mathrm{e0} c_2}{N_\mathrm{t,max}} \right|^{n_\mathrm{int}} \right)^{\frac{1}{p_\mathrm{int}} - 1}} \frac{\left| \frac{N_\mathrm{e0} c_1}{N_\mathrm{n,max}} \right|^{q_\mathrm{int} - 1}}{\left| \frac{N_\mathrm{e0} c_2}{N_\mathrm{t,max}} \right|^{n_\mathrm{int} - 1}}. \tag{3}$$

The incremental changes in position and angle (dx_i, dz_i, and $d\theta_{\mathrm{a},i}$) are calculated according to:

$$\begin{aligned} dx &= ds\cos(\theta_\mathrm{f}) + ds R_\mathrm{nt0}\sin(\theta_\mathrm{f}) \\ dz &= ds\sin(\theta_\mathrm{f}) - ds R_\mathrm{nt0}\cos(\theta_\mathrm{f}) \\ d\theta_a &= d\theta_{a_{dz}} dz. \end{aligned} \tag{4}$$

A detailed description of the parameters used in Eqs. (3) and (4) is given by Dao et al. (2024b,a).

The results obtained by the embedment calculations are shown in Fig. 9. Fig. 10 shows the maximum embedment depths for the varied fluke and shank lengths, with the optimum result being S3 with $L_\mathrm{f} = L_\mathrm{s} = 4\,\mathrm{m}$ corresponding to the same geometry of S2. The resulting single-objective DEAs S1, S2, and S3 are presented in Fig. 11.

Comparison to field data

Fig. 12 presents a comparison conducted by Aubeny (2017) between back-analyses using the described model and field data from five instrumented anchor installations. Measurements include both continuous tracking of horizontal and vertical anchor positions and discrete observations, such as the final anchor position after installation. The anchors examined are Vryhof and Bruce anchors. To ensure consistent comparison between calculated and measured trajectories, offsets were applied in both horizontal and vertical directions. Information regarding anchor geometry, mooring line properties, estimated soil strength profiles, and other relevant test details is provided by Yoon (2002) and Kim (2007), while the model parameters used in the back-analyses are summarised by Aubeny (2017). The comparison demonstrates that the model yields realistic predictions of anchor behaviour during installation.

With the governing equations established, the problem can now be formulated as a multi-objective optimisation task aiming to minimise the anchor volume V while maximising both the bearing factor $N_\mathrm{e,max}$ and the embedment depth z_max. The following section outlines the optimisation algorithm used to solve this problem.

3. Genetic optimisation algorithm and multi-objective approach for DEA optimisation

This section describes the gamultiobj algorithm in MATLAB applied in this study, which has been developed based on the NSGA-II by Deb et al. (2002a) for solving multi-objective optimisation problems. Crucial features of gamultiobj based on MathWorks (2025b) and Deb et al. (2002a), such as population management, selection mechanisms, and diversity control metrics like crowding distance and spread, are discussed in the following to provide insight into the methodology and the choice of optimisation parameters.

Population and evaluation

A population-based approach was followed in this study. A random initial population of candidate solutions was generated within the defined decision variable bounds. Each individual represented a solution vector $\mathbf{x} = (x_1, x_2, \ldots, x_n) \in \mathbb{R}^n$, where n denotes the number of decision variables. The evaluation process maps each individual to a vector of objective values that defines the following minimisation problem:

$$\min_{\mathbf{x}\in\mathbb{R}^n} \left\{ f_1(\mathbf{x}), f_2(\mathbf{x}), \ldots, f_m(\mathbf{x}) \right\}. \tag{5}$$

Initial population

A starting population of size N is generated randomly within the decision variable bounds:

$$x_{i,k} \sim U\left(x_k^\mathrm{min}, x_k^\mathrm{max}\right), \; i = 1, \ldots, N, k = 1, \ldots, n. \tag{6}$$

Here, $x_{i,k}$ denotes the kth decision variable of individual i, x_k^min and x_k^max denote the corresponding bounds and $U\left(x_k^\mathrm{min}, x_k^\mathrm{max}\right)$ denotes the uniform distribution between the bounds. Fig. 13 shows a randomly selected population of individuals in the decision variable space for $n = 2$, within the bounding box $[x_1^\mathrm{min}, x_1^\mathrm{max}] \times [x_2^\mathrm{min}, x_2^\mathrm{max}]$. The figure also shows the evaluation for two objective functions, $f_1(x_1, x_2)$ and $f_2(x_1, x_2)$ in the objective space.

After the initial population of size N is generated and all objective values are evaluated, a non-dominated sorting is performed on these N individuals, and the crowding distance d_i for each individual is computed. The algorithm then assigns front ranks and crowding distances, followed by the selection of parents for crossover and mutation via binary tournaments.

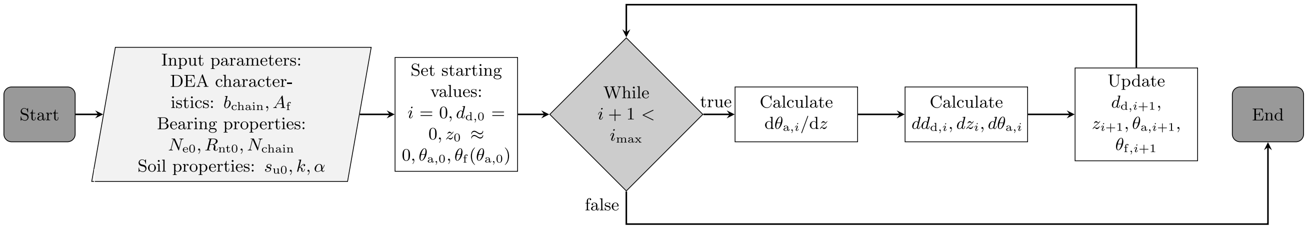

Fig. 8. Flowchart for computing embedment depth z: initialise iteration i, coordinates $d_{\mathrm{d},i}$, z_i, and angles $\theta_{\mathrm{a},0}$, $\theta_{\mathrm{f},0}$; compute $\mathrm{d}\theta_{a,i}/\mathrm{d}z$ and increments $dd_{\mathrm{d},i}$, dz_i, $d\theta_{\mathrm{a},i}$; update $d_{\mathrm{d},i+1}$, z_{i+1}, $\theta_{\mathrm{a},i+1}$, $\theta_{\mathrm{f},i+1}$; repeat until $i+1 = i_{\max}$.

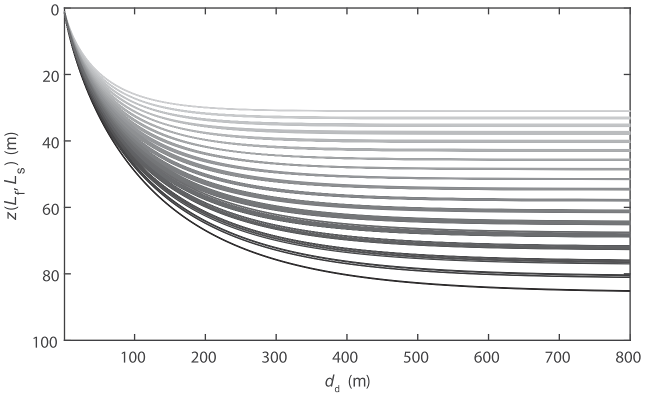

Fig. 9. Embedment depth $z(L_{\mathrm{f}}, L_{\mathrm{s}})$ over dragging distance d_{d}.

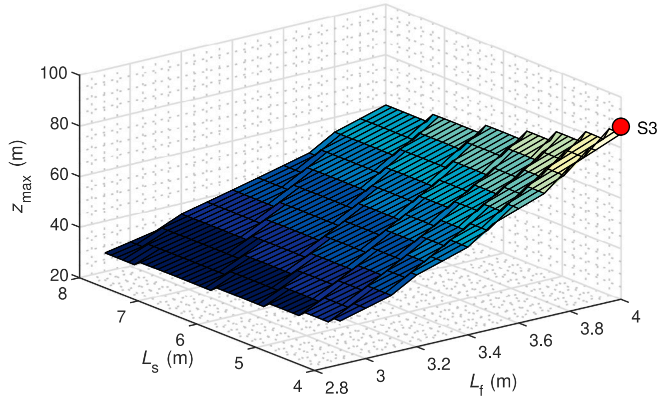

Fig. 10. Maximum embedment depth $z_{\max}$ as a function of fluke length L_{f} and shank length L_{s}, including the single-objective embedment depth-optimal solution (S3).

Non-dominated sorting

Once all objective values are evaluated as shown in Fig. 13, individuals are ranked using non-dominated sorting. A solution $\mathbf{x}$ dominates another solution $\mathbf{y}$ if it satisfies:

$$\begin{aligned} &\forall i \in \{1, \ldots, m\} : f_i(\mathbf{x}) \leq f_i(\mathbf{y}) \\ &\qquad \text{and} \\ &\exists j \in \{1, \ldots, m\} : f_j(\mathbf{x}) < f_j(\mathbf{y}). \end{aligned} \tag{7}$$

The first front consists of non-dominated individuals, while subsequent fronts contain individuals with increasing levels of domination. Fig. 14 illustrates the non-dominant sorting and the corresponding assignment of ranks to individuals, indicated by the colours of the fronts in the objective space.

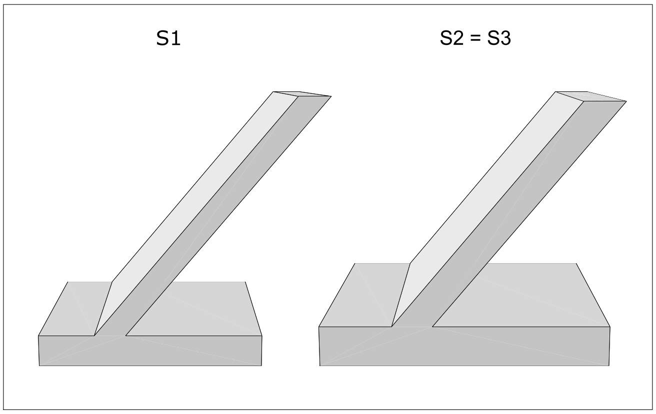

Fig. 11. Single-objective optimal anchor forms regarding V, $z_{\max}$ and $N_{\mathrm{e,max}}$.

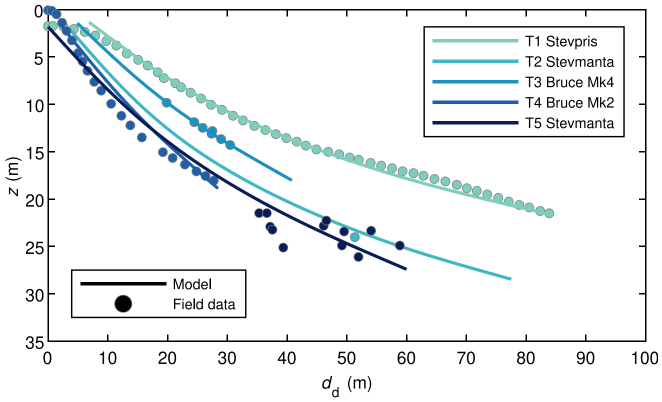

Fig. 12. Comparison of semi-analytical solution with field data, showing the variation of penetration depth z with respect to drag distance d_{d}. All data are obtained from Aubeny (2017).

Crowding distance computation

To promote sufficient diversity, a crowding distance metric is used for each individual, which is defined as:

$$d_i = \sum_{j=1}^{m} \frac{f_j^{(i+1)} - f_j^{(i-1)}}{f_j^{\max} - f_j^{\min}}. \tag{8}$$

Here, $f_j^{(i+1)}$ and $f_j^{(i-1)}$ are neighbouring objective values in front j, and $f_j^{\max}, f_j^{\min}$ are the extremas in that front. Based on the front belonging or rank and the corresponding crowding distance, the individuals or parents for the crossover and mutation are selected. Individuals with larger crowding distances are preferred, as they contribute to maintaining diversity along the Pareto front.

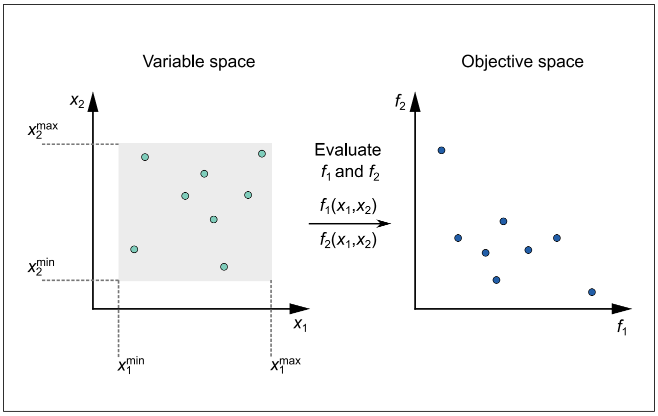

Fig. 13. Evaluation of a randomly initialised population of individuals.

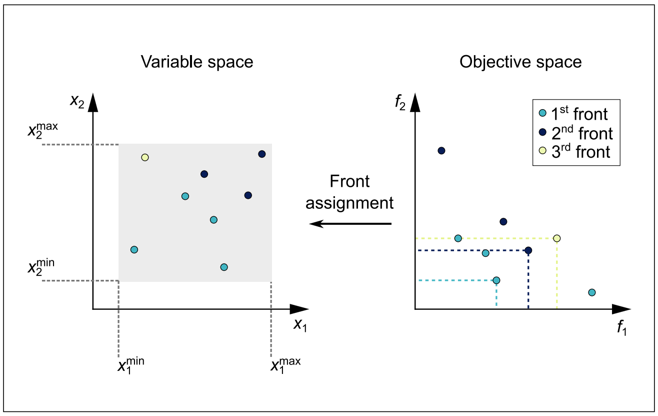

Fig. 14. Non-dominated and the ranking in different fronts.

Parent selection

Parents are chosen using binary tournament selection with rank, where Pareto front numbers are used, with lower numbers being preferred. The crowding distance d_i is used as a tie-breaker. If two candidates have equal rank, the one with larger d_i is selected. The parents are then used to create additional individuals, referred to as children. The total number of N children is generated by crossover and mutation.

Crossover

One fraction of the children is created by crossover and the other by mutation. The sizes of the fractions are controlled by the crossover fraction parameter ρ_c:

$$\begin{aligned} N_{\text{offspring}} &= \lfloor \rho_c \cdot N \rfloor, \\ N_{\text{mutation}} &= N - N_{\text{offspring}}. \end{aligned} \tag{9}$$

Arithmetic crossover of two parents $\mathbf{x}^{(1)}$ and $\mathbf{x}^{(2)}$ produces the children:

$$\begin{aligned} \mathbf{x}'^{(1)} &= \alpha \mathbf{x}^{(1)} + (1-\alpha)\mathbf{x}^{(2)}, \\ \mathbf{x}'^{(2)} &= \alpha \mathbf{x}^{(2)} + (1-\alpha)\mathbf{x}^{(1)}, \\ &\text{for an } \alpha \sim U(0,1) \end{aligned} \tag{10}$$

where $U(0,1)$ denotes the uniform distribution on $[0,1]$.

Feasible mutation

For the remaining N_{mutation} children, the mutation perturbs every decision variable by a small random amount while ensuring that the resulting solution remains within its bounds. The perturbation $\Delta_{i,k}$ is randomly chosen for each component k of an individual i and added additively.

Table 2
Input parameters for the optimisation algorithm.

Parameter	Value
Initial population size	800
Maximal number of generations	2000
Pareto fraction	0.7
Crossover fraction	0.95
Mutation adaptive feasibility	0.1
Function tolerance	1×10^{-6}
Maximal stall generations	100

$$\Delta_{i,k} \sim U(-\varepsilon_{i,k}, \varepsilon_{i,k}) \implies y_{i,k} = x_{i,k} + \Delta_{i,k}, \tag{11}$$

where $U(-\varepsilon, \varepsilon)$ denotes the uniform distribution on $[-\varepsilon, \varepsilon]$. To enforce feasibility, $x_{i,k}^{\min} \leq x_{i,k} \leq x_{i,k}^{\max}$, with respect to lower and upper bounds the clip function is used:

$$\begin{aligned} x'_{i,k} &= \operatorname{clip}(y_{i,k};\, x_i^{\min},\, x_{i,k}^{\max}) \\ &= \min\big(\, \max(y_{i,k},\, x_{i,k}^{\min},\, x_{i,k}^{\max}\,)\,\big)\,. \end{aligned} \tag{12}$$

The enforcement guarantees that each mutated variable $x'_{i,k}$ stays within the allowed interval $[x_{i,k}^{\min}, x_{i,k}^{\max}]$.

The crossover and mutation processes generate N new individuals, in addition to the N individuals in the initial population. All the individuals are sorted using the non-dominant sorting algorithm in Eq. (7), after which the crowding distance as shown in Eq. (8) is computed. As in the parent selection process, the best N individuals are chosen for the next iteration. The process is achieved by filling the slots with individuals of the fronts $F_1, F_2, \ldots$ until the size reaches N. If the last front F_L only partially fits, the top individuals with the largest d_i are selected.

Pareto fraction

The Pareto fraction parameter implements elitism with respect to Pareto dominance by reserving a proportion of the next generation directly from the best non-dominated solutions. After non-dominated sorting is applied, the number of elite individuals preserved without modification is defined as:

$$N_{\text{elite}} = \lfloor \text{Pareto fraction} \cdot N \rfloor, \tag{13}$$

where N is the target population size for the next generation. These N_{elite} individuals are selected by taking whole fronts in increasing rank order (starting from F_1). The remainder of the population, $N - N_{\text{elite}}$, is filled by selecting from the remaining individuals in R according to their front rank and crowding distance, possibly involving recombined or mutated solutions.

Monitoring convergence and spread

After each generation, the algorithm computes two metrics on the current best front F_1 of size $|F_1|$. Each solution $\mathbf{x}_i$ has the objective vector

$$f(\mathbf{x}_i) = \big(f_1(\mathbf{x}_i),\, f_2(\mathbf{x}_i),\, \ldots,\, f_m(\mathbf{x}_i)\big)^{\top}. \tag{14}$$

The centroid of F_1 in objective space is defined as:

$$\bar{f} = \frac{1}{|F_1|} \sum_{i \in F_1} f(\mathbf{x}_i). \tag{15}$$

The convergence is measured by the value C, the average Euclidean distance of front points to the centroid:

$$\begin{aligned} C &= \frac{1}{|F_1|}\sum_{i\in F_1}\left\| f(\mathbf{x}_i) - \bar{f}\right\|_2 \\ &= \frac{1}{|F_1|}\sum_{i\in F_1}\sqrt{\sum_{j=1}^{m}\left(f_j(\mathbf{x}_i) - \bar{f}\right)^2}. \end{aligned} \tag{16}$$

The spread S quantifies additionally the extent of the front i by its maximum pairwise distance:

$$\begin{aligned} S &= \max_{i,j\in F_i}\left\| f(\mathbf{x}_i) - f(\mathbf{x}_j)\right\|_2 \\ &= \max_{i,j}\sqrt{\sum_{k=1}^{m}\left(f_k(\mathbf{x}_i) - f_k(\mathbf{x}_j)\right)^2}. \end{aligned} \tag{17}$$

The per-individual distance d_i is a further metric to characterise the isolation or clustering of different solutions and is defined as the minimum Euclidean distance (nearest neighbour) of each solution as:

$$d_i = \min_{j\neq i}\left\| f(\mathbf{x}_i) - f(\mathbf{x}_j)\right\|_2. \tag{18}$$

The metrics are displayed at each iteration and used as stopping criteria (e.g., function tolerance) for the optimisation process in the following section.

4. Case studies

To demonstrate the functionality of the optimisation framework, this section presents three case studies. Case study 1 analyses the boundaries of the variable space. Case Study 2 investigates how the Pareto front changes when different parameters are selected as decision variables. Case study 3 introduces a new objective function, which is formed as a weighted sum of the initial objective functions to identify a case-specific solution. For the case studies presented in the following paragraphs, the set of optimisation parameters is summarised in Table 2.

The population size and the number of generations were set to relatively high values to improve robustness against premature convergence and to ensure adequate exploration of the design space. This choice is motivated by the problem-specific characteristics of the optimisation, as the objective functions involve both analytical and numerical components, resulting in a highly nonlinear, potentially non-smooth search space. Parallelisation was enabled to maintain computational efficiency.

4.1. *Case study 1*

For case study 1, the optimisation algorithm is applied for the parameters given in Table 1. The obtained V, N_e and z_{max} objective space, is presented in Fig. 15.

Since the optimisation procedure is stochastic, multiple independent runs are typically performed to obtain statistically robust results. However, the computational cost of the current optimisation is substantial. Each run requires approximately one day for three decision variables and 2000 generations with up to 24 CPU cores on a local machine. Due to this high computational demand, a full statistical evaluation with a larger number of runs, such as 30, was not performed. Instead, 15 independent runs with different initialisations were conducted. These runs consistently produced highly similar Pareto fronts and geometries, demonstrating stable convergence behaviour. Furthermore, a relatively large population size was selected to ensure broad coverage of the design space in the initial generation, thereby reducing sensitivity to random initialisation.

Figs. 16 and 17 show the convergence behaviour and diversity of the optimisation results. An average spread $\bar{S}$ of 0.44 indicates a relatively wide distribution of solutions along the Pareto front. Most distances between neighbouring individuals are below 0.01, suggesting a high level of clustering and reliable convergence in large parts of the front, also covering a broader range of alternatives. Only a few gaps up to 0.12 were observed, indicating that the chosen sample was sufficiently large.

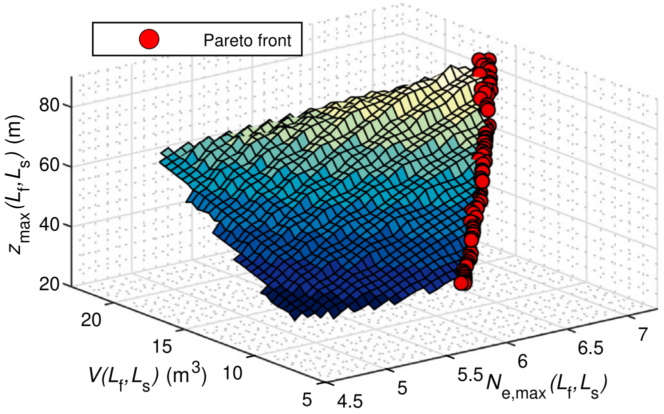

Fig. 15. Solution set of the conducted DEA analysis Pareto front.

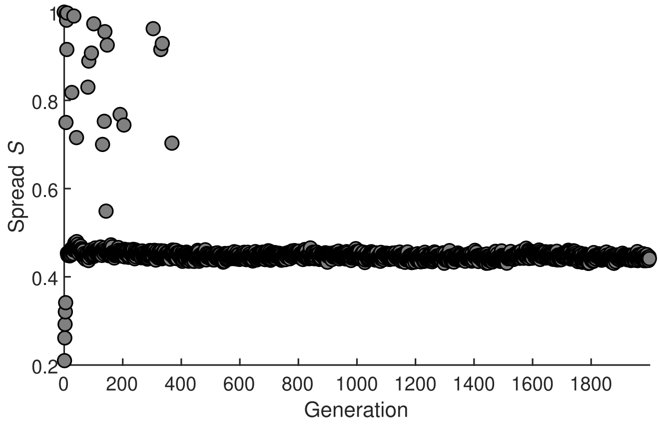

Fig. 16. Spread over each generation.

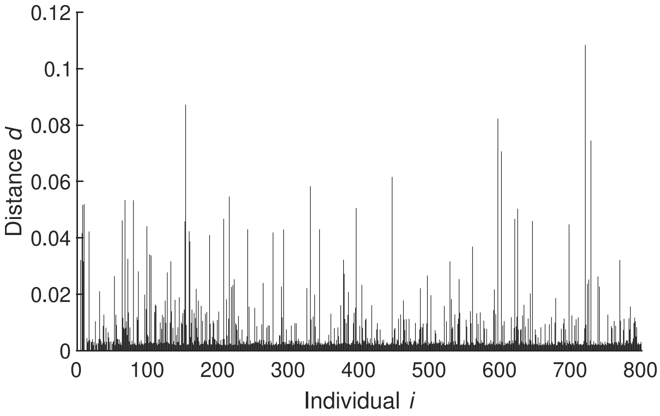

Fig. 17. Distance of Individuals.

All Pareto optima are positioned at the boundary of the solution space (Fig. 15), suggesting that the lower and upper constraints of L_f and L_s may play a decisive role in defining the Pareto-optimal solutions. The fluke and shank length relationship is shown in the $L_{f,opt}$-$L_{s,opt}$ diagram in Fig. 18, where the fluke and the shaft length of the Pareto-optimal solutions corresponding to different boundary

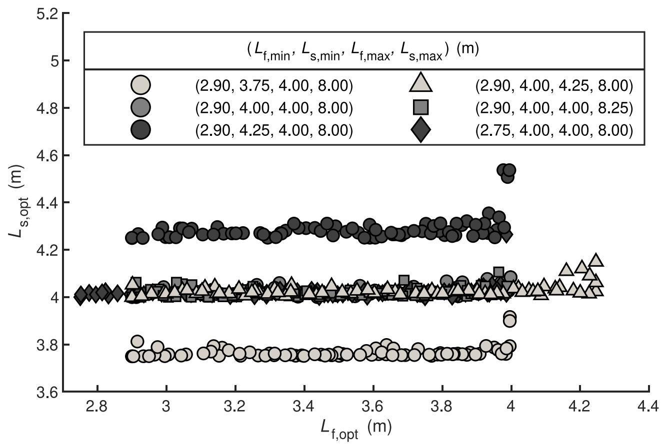

Fig. 18. Solution set of the conducted DEA analysis Pareto front.

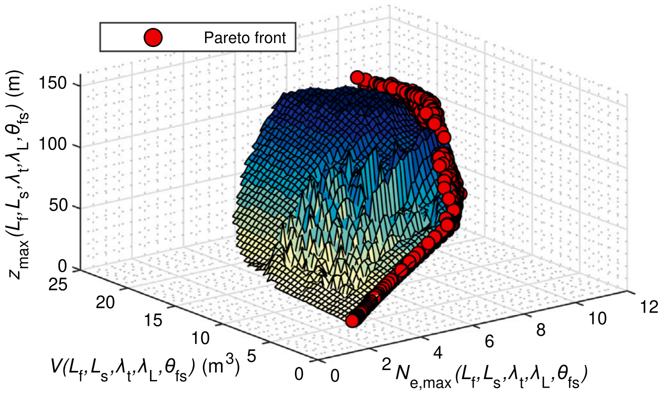

Fig. 19. Pareto front of DEA analysis parametrised for L_f, L_s, λ_t, λ_L and θ_{fs}.

Table 3
Input parameters for volume and bearing capacity factor analysis.

Parameter	Value	Unit	Definition
L_f	2.9 to 4.0	m	Fluke length
L_s	4 to 8	m	Shank length
t_f	$\lambda_t L_f$	m	Fluke thickness
λ_t	0.1 to 0.2	–	Thickness factor
L_j	$\lambda_L L_f$	m	Junction length
λ_L	0.2 to 0.3	–	Junction length factor
θ_{fs}	30 to 60	°	Fluke-shank angle

conditions are plotted. To analyse the influence of the constraints, the upper and lower boundaries of L_f and L_s were systematically varied. The results show that increasing the upper boundaries does not affect the location of the Pareto-optimal solutions. Likewise, modifying the lower boundary of L_f does not alter the Pareto-optimal region either. Only an increase in the lower boundary of L_s leads to a shift in the location of the Pareto-optimal solutions. Overall, the boundary analysis shows that some Pareto-optimal solutions may fall outside the current variable space and that by excluding certain boundaries that do not influence the results, the solution space can be reduced for an efficient optimisation.

4.2. Case study 2: Parameterisation of additional anchor geometries

In this case, further anchor geometries are parametrised to identify Pareto-optimal anchor shapes. The additionally considered parameters include the fluke-shank angle θ_{fs}, the joint length L_j controlled by the factor λ_L, and the fluke thickness t_f controlled by the factor λ_t. The parameter ranges used for this case are provided in Table 3. All other geometric properties remain unchanged, as defined in 1.

Fig. 19 illustrates that the algorithm successfully identified Pareto-optimal solutions along the Pareto front within the defined solution space. The Pareto-optimal points of the extended DEA analysis, which incorporates additional decision variables, also consistently occur at the boundary of the solution space. Although the Pareto front covers a large portion of the possible solutions for z_{max} and $N_{e,max}$, a dominance of solutions with a volume below 10 m^3 is observed. A more detailed representation of the parameter behaviour is shown in the radar chart in Fig. 20.

To compare each decision variable directly, the axes were normalised using a min–max normalisation applied globally across the full dataset of 560 Pareto-optimal individuals. Normalisation was done individually for each of the five decision variables (L_f, L_s, θ_{fs}, λ_t, λ_L). The minimum values were subtracted from the observed values, and the result was divided by the range of that decision variable. The procedure mapped all values to the interval $[0, 1]$.

To identify distinct groups, hierarchical clustering with Ward's minimum-variance linkage was applied to all Pareto-optimal geometries. By finding the smallest increase in overall within-cluster variance, the method produces clusters that are as homogeneous as possible (i.e., points within each cluster are similar to each other) (Ward Jr., 1963). The resulting dendrogram was cut to yield three distinguishable clusters, with a low Davies–Bouldin index of 0.73, indicating well-separated, compact clusters (Davies and Bouldin, 2009). The final cluster sizes are $n_{C1} = 242$, $n_{C2} = 232$, and $n_{C3} = 86$.

- **Cluster 1** ($n_{C1} = 242$) has large values in L_s, L_f, λ_t and θ_{fs}, but a comparatively small λ_L. In terms of anchor geometry, the Cluster 1 solutions correspond to a wide fluke–shank section and thick flukes combined with a high fluke–shaft angle and a relatively small junction area.
- **Cluster 2** ($n_{C3} = 232$) is defined by strong peaks in L_f, λ_t and θ_{fs}, while L_s and λ_L remain moderate. The Cluster 2 solutions combine large flukes and thickness with a high fluke–shaft angle.
- **Cluster 3** ($n_{C2} = 86$) shows pronounced peaks either only in λ_L or in both λ_L and θ_{fs}.

Fig. 21 illustrates three anchor geometries representative of each cluster. A high fluke–shank angle θ_{fs} observed across all clusters is consistent with practical experience of greater embedment and higher load efficiency at larger angles in clay (Delmar, 2018). The cluster patterns align with established mechanics of drag and plate type anchors: resistance scales with the soil reaction mobilised normal to the load and the projected fluke area, moderated by bearing factors (O'Neill et al., 2003; Aubeny and Chi, 2010; Zhou et al., 2020; Roy et al., 2022; Gaudin et al., 2006). Thus, geometries with broader and thicker flukes are expected to deliver higher capacity, at the cost of increased volume. Clusters 2 and 3 follow this area-driven trend, whereas Cluster 1 reflects a capacity–volume trade-off by limiting junction length while retaining favourable fluke dimensions and angle.

Interpretation of the identified clusters must account for the underlying modelling assumptions. The semi-analytical framework is valid primarily within the geometric ranges examined in physical and numerical studies. Therefore, extreme geometries should be considered with caution. Furthermore, practical constraints such as installation stability, including fluke-shank angle, and the assumed soil strength profile may affect the applicability of the identified optimal configurations. Further discussion of these aspects is provided in Section 4.4.

Figs. 22 and 23 indicate good convergence and acceptable diversity. An average spread $\bar{S}$ of 0.20 reflects a moderately uniform distribution of solutions along the Pareto front. Most distances between neighbouring individuals were below 0.01, suggesting a high degree of clustering and reliable convergence. The convergence metrics further indicate

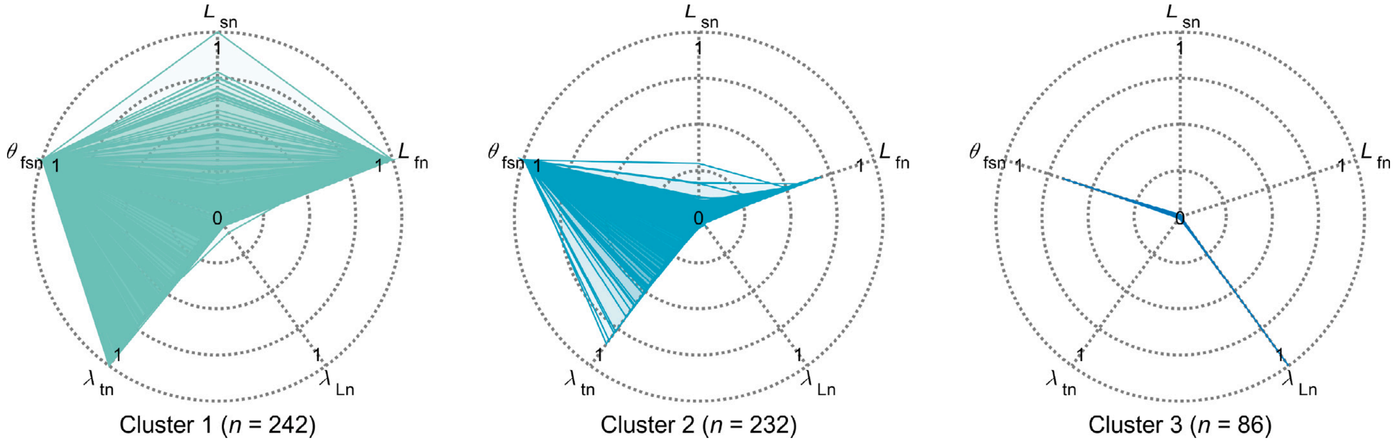

Cluster 1 (n = 242)

Cluster 2 (n = 232)

Cluster 3 (n = 86)

Fig. 20. Pareto-optimal parameters in L_f-L_s-λ_t-λ_L-θ_{fs} space.

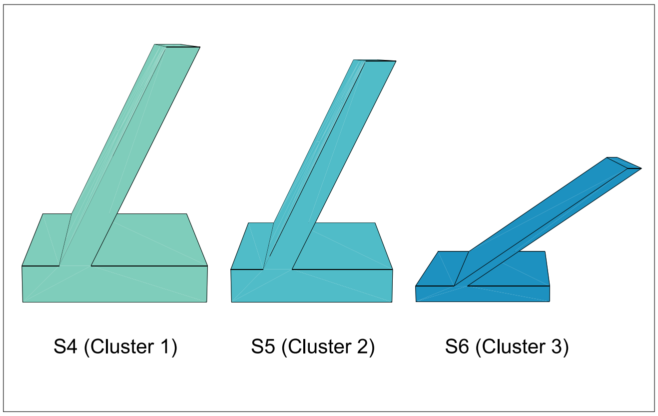

Fig. 21. Examples of the optimised anchor forms in the scope of this study.

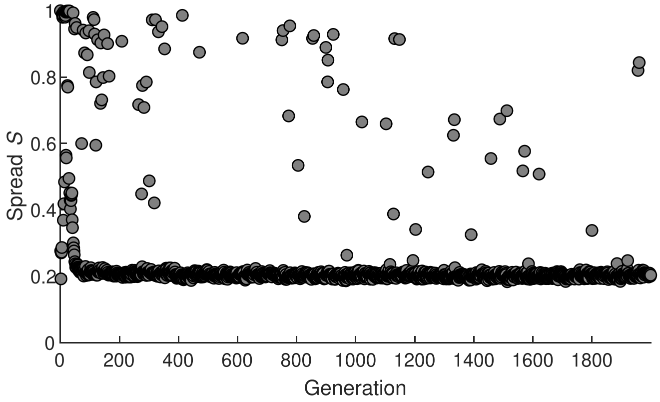

Fig. 22. Average spread $\bar{S} = 0.203283$.

that the optimisation process stabilised after approximately 500 generations, as no significant changes in the Pareto front or its spacing were observed beyond this point. The optimisation was still continued up to 2000 generations to verify the robustness of the results and to confirm that no further improvements or transitions to alternative solution regions occurred.

4.3. Case study 3: Finding a single optimal solution from the multi-objective optimisation

In the previous two case studies, multiple possible optima were identified. A scalar objective function containing all relevant objectives maps each design to a single scalar value by combining its individual performance metrics through user-defined weights. The scalarisation enables the selection of a specific solution by tuning the relative importance of competing criteria.

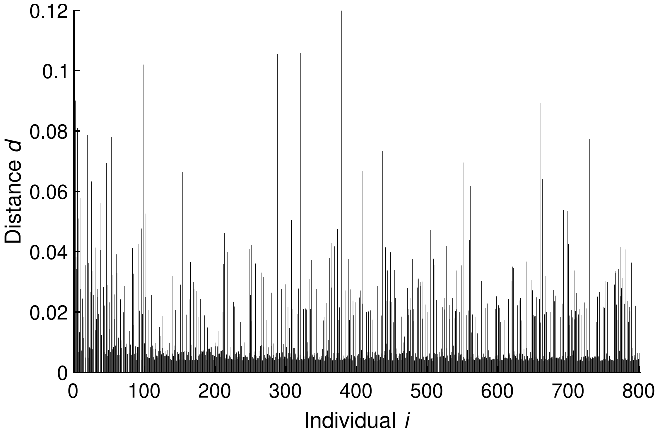

Fig. 23. Distance of individuals.

To select a single compromise design, an objective function $K(\mathbf{x})$, that combines anchor volume V, bearing factor $N_{\mathrm{e,max}}$ and embedment depth $z_{\max}$, is introduced. Each design $\mathbf{x}$ is evaluated by

$$\begin{aligned} K(\mathbf{x}) \;=\; & w_V\, V_{\mathrm{n}}(\mathbf{x}) \;+\; w_z\left[1 - z_{\mathrm{max,n}}(\mathbf{x})\right] \\ & +\; w_N\left[1 - N_{e,\mathrm{max,n}}(\mathbf{x})\right], \end{aligned} \tag{19}$$

where w_V, w_z, and w_N are user-defined weights that adjust the emphasis on material usage, embedment depth, and bearing factor, respectively, and the subscript n indicates normalised values. The weights could be coupled with actual costs. By construction, larger embedment depth and bearing factor reduce the corresponding terms in K, whereas larger volume increases the first term. In this study $w_V = w_z = w_N$ are set to 1, yielding

$$K(\mathbf{x}) = V_{\mathrm{n}}(\mathbf{x}) + \left[1 - z_{\mathrm{max,n}}(\mathbf{x})\right] + \left[1 - N_{e,\mathrm{max,n}}(\mathbf{x})\right]. \tag{20}$$

The new optimisation problem is to minimise $K(\mathbf{x})$. This single-objective problem can be solved using various methods, including genetic algorithms. The corresponding single optimal solution identified by the objective function (white triangle) is presented in Fig. 24. The solution lies within the Pareto front of the multi-objective problem. This is the case when the weights are positive numbers. Conversely, not every Pareto-optimal solution can always be represented as the minimum of a weighted sum.

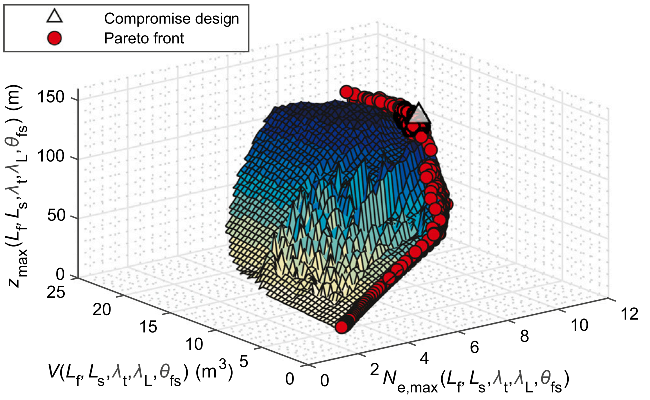

Fig. 24. Solution set of the conducted DEA analysis with Pareto front and weighted single optimum.

4.4. Limitations

As with any evolutionary optimisation, the outcome depends on parameter selection and algorithm configuration, such as crossover and mutation rates, population size, and termination criteria. Although these settings can be managed with sufficient attention, the results are predominantly determined by the underlying equations that describe DEA behaviour, rather than by the optimisation algorithm itself.

The study applies a frequently used simplified geometric model of a DEA in combination with a single set of soil parameters, which reduces the number of variables and the complexity of the objective functions.

The semi-analytical framework adopted in this study is primarily valid within geometric ranges that have been investigated in physical model and field tests. Extreme geometries, such as exceptionally long or thick flukes, fall outside this validated range and should therefore be interpreted with caution. For example, previous numerical studies have demonstrated that variations in fluke width can influence embedment behaviour, with larger fluke widths increasing anchor rotation and leading to less stable embedment paths (Zhang et al., 2023).

In addition, the fluke-shank angle has been identified as a critical design parameter. While optimisation suggests that larger angles may enhance performance, excessively large angles can cause instability during embedment or reduce penetration efficiency, as demonstrated in physical model tests by Liu et al. (2010). Therefore, geometric feasibility and installation stability impose practical constraints that are not fully addressed in the current formulation.

Soil conditions are represented by a simplified undrained shear strength profile with a constant gradient. Due to geometric nonlinearities associated with large rotations and the coupling between embedment depth and projected area, the system response does not vary linearly with the strength gradient. Variations in the gradient may influence both the absolute capacity and the relative performance of different geometries. A comprehensive parametric study is required to evaluate the robustness of the identified optimal configurations with respect to changes in shear strength gradient.

More complex soil conditions, such as layered or spatially variable profiles (Peng et al., 2021; Lai et al., 2025b), were not considered and may further influence anchor behaviour. The presented workflow allows for the integration of such complexities, including more advanced modelling approaches for soil–anchor interaction (e.g., numerical methods, contact formulations, or advanced constitutive models Ma et al., 2022; Singh et al., 2021, 2023; Liu et al., 2021; Dao et al., 2025b), as well as extended design spaces that incorporate additional geometric parameters.

5. Conclusions and outlook

This study presents a framework for optimising the geometry of DEAs for floating offshore structures, considering various objectives simultaneously, by using a multi-objective evolutionary algorithm. The presented approach enables the identification of anchor designs that minimise volume while maximising bearing capacity and penetration depth. The results show that suboptimal designs can be excluded and improved boundaries for the design parameters can be established. The generated Pareto front enables users to identify case-specific solutions, either by directly selecting from the Pareto front or by applying a single-objective optimisation with a weighted objective function. For the parameters considered in this study, three distinct design clusters were identified, which can be interpreted as three types of anchor designs. These findings indicate that additional decision variables and objective functions can be incorporated into the optimisation process in future work. The proposed framework also allows the parameter ranges to be further refined as new variables are introduced. Scaled prototype tests can be conducted based on these results, and the process may be extended through numerical simulations to validate and refine the findings. Finally, the simple anchor model applied in the framework can be further developed, made more complex, or replaced with other approaches, as the framework is applicable to any anchor design formulation.

CRediT authorship contribution statement

D.A. Dao: Writing – review & editing, Writing – original draft, Visualization, Validation, Supervision, Software, Resources, Project administration, Methodology, Investigation, Formal analysis, Data curation, Conceptualization. **A. Chmelnizkij:** Writing – review & editing, Writing – original draft, Visualization, Validation, Supervision, Software, Resources, Project administration, Methodology, Investigation, Formal analysis, Data curation, Conceptualization. **K. Cerek:** Writing – review & editing, Validation, Software, Methodology, Conceptualization. **E. Hadjiloo:** Writing – review & editing, Validation, Software, Methodology, Conceptualization. **J. Grabe:** Writing – review & editing, Validation, Resources, Funding acquisition. **K. Smarsly:** Writing – review & editing, Validation, Resources, Funding acquisition.

Declaration of competing interest

The authors declare that they have no known competing financial interests or personal relationships that could have appeared to influence the work reported in this paper.

Acknowledgements

This study was supported by the German Research Foundation (DFG), under grant GR 1024/61-1. The authors express their gratitude for the financial assistance provided.

Nomenclature

Symbol/abbreviation	Description
A_f	Fluke area
b_chain	Line diameter
C	Convergence
c_i	Coefficient
DEA	Drag embedment anchor
d_d	Horizontal position
dd_d	Incremental change in horizontal position
dz	Incremental change in depth
$d\theta_a$	Incremental change in anchor line angle
E_n	Multiplier
f	Function for interaction of forces and moment at centre of fluke
f_i	Objective function
F_n	Normal loading
FOWT	Floating offshore wind turbine
F_t	Tangential loading
i	Iteration count
k	Strength gradient
$K(\mathbf{x})$	Objective function
L_c	Centre length
L_ca	Geometric auxiliary parameter
LDFE	Large-deformation finite element (analysis)
L_f	Fluke length
L_j	Junction length
L_s	Shank length
M	Moment
m_int	Interaction coefficient
N	Population size
n	Number of decision variables
n_int	Interaction coefficient
n_{Ci}	Cluster size
N_chain	Chain bearing capacity factor
N_e	Bearing capacity factor
N_e0	Rotational-neutral bearing capacity factor
$N_\mathrm{e,max}$	Maximum bearing capacity factor
N_et	Bearing capacity factor with only tangential loading
$N_\mathrm{m,max}$	Normalised maximum bearing capacity factor (moment)
$N_\mathrm{n,max}$	Normalised maximum bearing capacity factor (normal loading)
$N_\mathrm{t,max}$	Normalised maximum bearing capacity factor (tangential loading)
NSGA-II	Non-dominated sorting genetic algorithm II
p_int	Interaction coefficient
q_int	Interaction coefficient
R_nt0	Ratio of normal to tangential translation
s_u0	Mudline shear strength
SSI	Structure-soil interaction
S_t	Sensitivity
t_f	Fluke thickness
t_f	Shank thickness
V	Anchor volume
w	User-defined weight
w_f	Fluke width
w_s	Shank width
$\mathbf{x}$	Solution vector
$x'^{(i)}$	Child
$x^{(i)}$	Parent
$x_{i,k}$	k^th decision variable of individual i
$\mathbf{y}$	Solution vector
y_i	Individual solution
z	Embedment depth
α	Adhesion coefficient
Δ_i	Perturbation
$\theta_\mathrm{a,0}$	Initial anchor line angle
θ_af	Loading angle
θ_ca	Geometric auxiliary parameter
$\theta_\mathrm{f,0}$	Initial fluke angle
θ_fs	Fluke-shank angle
λ_L	Junction length factor
λ_t	Thickness factor
ρ_c	Crossover fraction parameter

References

ABS, 2018. Guidance Notes - Design and Installation of Drag Anchors and Plate Anchors. American Bureau of Shipping.

Amanat, S., Gholami, K., Rafiee-Dehkharghani, R., Bansal, D., 2023. Modified non-dominated sorting genetic algorithm-II for the optimal design of soil-concrete periodic plane wave barriers. Comput. Geotech. 160, 105947. http://dx.doi.org/10.1016/j.compgeo.2023.105947.

An, N., Wang, G., Wang, D., Ma, G., Chang, X., Zhou, W., 2025. DEM parameter calibration based on multi-objective Bayesian optimization and prior physical information. Acta Geotech. http://dx.doi.org/10.1007/s11440-025-02537-7.

Aubeny, C., 2017. Geomechanics of Marine Anchors. CRC Press.

Aubeny, C.P., Chi, C., 2010. Mechanics of drag embedment anchors in a soft seabed. J. Geotech. Geoenvironmental Eng. 136 (1), 57–68.

Aubeny, C.P., Gilbert, R., Randall, R., Zimmerman, E., McCarthy, K., Chen, C.-H., Drake, A., Yeh, P., Chi, C.-M., Beemer, R., 2011. The Performance of Drag Embedment Anchors (DEA). Texas A&M University.

Cerek, K., Grabe, J., 2022. Numerical simulation and optimization of dike geometry using multi-objective evolutionary algorithm NSGA-II. ISSMGE http://dx.doi.org/10.53243/NUMGE2023-80.

Cerek, K., Hadjiloo, E., Grabe, J., 2024. Sustainable dike adaptation measures using finite element method and optimization algorithm NSGA-II. In: Proceedings of the 5th International Conference on Geotechnics for Sustainable Infrastructure Development. Springer Nature Singapore, Singapore, pp. 2077–2091. http://dx.doi.org/10.1007/978-981-99-9722-0_139.

Cerek, K., Hadjiloo, E., Grabe, J., Dao, D.A., 2025. Optimization of drag embedment anchors applying multi-objective evolutionary algorithm NSGA-II. J. Ocean Eng. Sci. 10 (6), 1019–1030. http://dx.doi.org/10.1016/j.joes.2025.07.002.

Cerfontaine, B., White, D., Kwa, K., Gourvenec, S., Knappett, J., Brown, M., 2023. Anchor geotechnics for floating offshore wind: Current technologies and future innovations. Ocean Eng. 279, 114327. http://dx.doi.org/10.1016/j.oceaneng.2023.114327.

Chmelnizkij, A., Dao, D.A., 2025. Duydaonow/deaoptimisation: MATLAB code for DEA optimisation. http://dx.doi.org/10.5281/ZENODO.16724837.

Dahlberg, R., 1998. Design Procedures for Deepwater Anchors in Clay. In: Offshore Technology Conference. OTC, Houston, Texas, pp. OTC–8837–MS. http://dx.doi.org/10.4043/8837-MS.

Dao, D.A., Alkateeb, D., Schröder, M., 2023. Discrepancies between element tests and large-scale LDFE simulations: A case study on anchor kinematics during installation in clay. Comput. Geotech. 163, 105698. http://dx.doi.org/10.1016/j.compgeo.2023.105698.

Dao, D.A., Cerek, K., Hadjiloo, E., Stager, T., 2024a. Parametrische Analyse des Eindringverhaltens und Identifizierung optimaler Geometrien von Ankern für schwimmende Offshore-Strukturen. In: 8. Baugrundtagung: Forum für Junge Geotechnik-Ingenieure und -Ingenieurinnen. Bremen, pp. 138–145.

Dao, D.A., Dicke, K., 2024. Numerical investigation of drag embedment anchor model reduction for FOWTs in coarse and fine-grained baltic sea soil. In: Proceedings of the 5th International Conference on Geotechnics for Sustainable Infrastructure Development. Springer Nature Singapore, Singapore, pp. 2871–2886. http://dx.doi.org/10.1007/978-981-99-9722-0_199.

Dao, D.A., Grabe, J., Chmelnizkij, A., 2024b. Examination of an analytical approach for load-displacement behavior of drag embedment anchors and their geometrical optimization. In: Volume 8: Offshore Geotechnics; Petroleum Technology. In: OMAE2024, American Society of Mechanical Engineers, http://dx.doi.org/10.1115/omae2024-124377, V008T10A011.

Dao, D.A., Grabe, J., da Silva, A.P., Langstraat, J., Su, Y.Y., Castelein, K., de Lange, D., Luger, D., van Eekelen, S., 2025a. Centrifuge modelling of anchor performance for floating offshore wind turbines: installation and load behaviour in sand. In: Proceedings of the 5th International Symposium on Frontiers in Offshore Geotechnics. ISFOG2025, pp. 2193–2198. http://dx.doi.org/10.53243/ISFOG2025-122.

Dao, D.A., Tafili, M., Williams-Riquer, F., Grabe, J., Wichtmann, T., 2025b. Large deformation simulations of structuresoil-interaction in anisotropic fine-grained soils. Comput. Geotech. 188, 107537. http://dx.doi.org/10.1016/j.compgeo.2025.107537.

Davies, D.L., Bouldin, D.W., 2009. A cluster separation measure. IEEE Trans. Pattern Anal. Mach. Intell. (2), 224–227. http://dx.doi.org/10.1109/TPAMI.1979.4766909.

Deb, K., Dhar, A., 2010. Optimum design of stone column-improved soft soil using multiobjective optimization technique. Comput. Geotech. 38 (1), 50–57. http://dx.doi.org/10.1016/j.compgeo.2010.10.005.

Deb, K., Pratap, A., Agarwal, S., Meyarivan, T., 2002a. A fast and elitist multiobjective genetic algorithm: NSGA-II. IEEE Trans. Evol. Comput. 6 (2), 182–197. http://dx.doi.org/10.1109/4235.996017.

Delmar, 2018. Vryhof manual - the guide to anchoring.

Dou, Y., Yu, L., 2018. Numerical investigations of the effects of different design angles on the motion behaviour of drag anchors. Appl. Ocean Res. 76, 199–210. http://dx.doi.org/10.1016/j.apor.2018.05.003.

Fan, J., Ferrell, B., O'Loughlin, C., Bransby, M.F., Watson, P., 2026. Combined 6-DoF motion tracking and photogrammetry to capture drag anchor installation behaviour in sand. In: Proceedings of the 11th International Conference on Physical Modelling in Geotechnics. ICPMG 2026, Zürich, Switzerland.

Gaudin, C., O'Loughlin, C.D., Randolph, M.F., Lowmass, A.C., 2006. Influence of the installation process on the performance of suction embedded plate anchors. Géotechnique 56 (6), 381–391. http://dx.doi.org/10.1680/geot.2006.56.6.381.

Gong, W., Luo, Z., Juang, C.H., Huang, H., Zhang, J., Wang, L., 2013. Optimization of site exploration program for improved prediction of tunneling-induced ground settlement in clays. Comput. Geotech. 56, 1–12. http://dx.doi.org/10.1016/j.compgeo.2013.10.008.

Gourvenec, S., 2024. Offshore geotechnical challenges of the energy transition. Geomech. Energy Environment 39, 100584. http://dx.doi.org/10.1016/j.gete.2024.100584.

Gras, J.-P., Sivasithamparam, N., Karstunen, M., Dijkstra, J., 2017. Strategy for consistent model parameter calibration for soft soils using multi-objective optimisation. Comput. Geotech. 89, 151–165. http://dx.doi.org/10.1016/j.compgeo.2017.06.006.

He, B.-H., Du, X.-L., Bai, M.-Z., Yang, J.-W., Ma, D., 2024. Inverse analysis of geotechnical parameters using an improved version of non-dominated sorting genetic algorithm II. Comput. Geotech. 167, 106416. http://dx.doi.org/10.1016/j.compgeo.2024.106416.

Khoshnoudian, F., Ayyobi, P., Paytam, F., Mirmo'azen, S.M., 2016. Genetic algorithm design of a soil–structure–damper system. Proc. Inst. Civ. Eng. - Struct. Build. 169 (10), 758–774. http://dx.doi.org/10.1680/stbu.14.00064.

Kim, B.M., 2007. Upper Bound Analysis for Drag Anchors in Soft Clay (Ph.D. thesis). Texas A&M University.

Lai, Y., Chen, C., Pan, A., Zhu, B., 2025a. Centrifuge modelling and the modified limit equilibrium prediction for drag embedment anchor installation in sand. Appl. Ocean Res. 154, 104390. http://dx.doi.org/10.1016/j.apor.2024.104390.

Lai, Y., Xiong, S., Wu, H., Xiu, X., Huang, Y., 2025b. A plasticity-based upper-bound prediction model incorporating shank effects for drag embedment anchor behavior in layered clay seabed. Comput. Geotech. 187, 107507. http://dx.doi.org/10.1016/j.compgeo.2025.107507.

Li, Z., Gong, W., Zhang, L., Wang, L., 2022. Multi-objective probabilistic back analysis for selecting the optimal updating strategy based on multi-source observations. Comput. Geotech. 143, 104959. http://dx.doi.org/10.1016/j.compgeo.2022.104959.

Liu, H., Liang, K., Peng, J., Xiao, Z., 2021. A unified explicit formula for calculating the maximum embedment loss of deepwater anchors in clay. Ocean Eng. 236, 109454.

Liu, H., Zhang, W., Zhang, X., Liu, C., 2010. Experimental investigation on the penetration mechanism and kinematic behavior of drag anchors. Appl. Ocean Res. 32 (4), 434–442. http://dx.doi.org/10.1016/j.apor.2010.09.004.

Ma, T., Xiao, Z., Zhang, W., Hu, P., Wei, X., 2022. Effect of the external beveled tip angle of the bucket foundation in clay on its penetration resistance considering soil large deformation and strain softening. Ocean Eng. 262, 112185.

MathWorks, 2025a. gamultiobj algorithm. (Accessed 27 July 2025), https://de.mathworks.com/help/gads/gamultiobj-algorithm.html.

MathWorks, 2025b. gamultiobj: Find Pareto front of multiple fitness functions using genetic algorithm. (Accessed 30 July 2025), https://de.mathworks.com/help/gads/gamultiobj.html.

MathWorks, 2025c. Genetic Algorithm Options. (Accessed 27 July 2025), https://de.mathworks.com/help/gads/genetic-algorithm-options.html.

Murff, J.D., 1994. Limit analysis of multi-footing foundation systems. In: Proceedings of the 8th International Conference on Computer Methods and Advances in Geomechanics. vol. 1, pp. 223–244.

Murff, J.D., Randolph, M.F., Elkhatib, S., Kolk, H.J., Ruinen, R., Strom, P., Thorne, C., 2005. Vertically loaded plate anchors for deepwater applications. In: Proceedings of the 1st International Symposium on Frontiers in Offshore Geotechnics. ISFOG2005, pp. 31–48.

Neubecker, S., Randolph, M.F., 1996. The performance of drag anchor and chain systems in cohesive soil. Mar. Georesources & Geotechnol. 14 (2), 77–96. http://dx.doi.org/10.1080/10641199609388305.

O'Neill, M.P., Bransby, M.F., Randolph, M.F., 2003. Drag anchor fluke soil interaction in clays. Can. Geotech. J. 40 (1), 78–94. http://dx.doi.org/10.1139/t02-096.

Peng, J., Liu, H., Liang, K., Xiao, Z., 2021. A theoretical model for analyzing the behavior of drag anchors in layered soils. Ocean Eng. 222, 108568.

Putuhena, H., White, D.J., Gourvenec, S., Sturt, F., 2023. Finding space for offshore wind to support net zero: A methodology to assess spatial constraints and future scenarios, illustrated by a UK case study. Renew. Sustain. Energy Rev. 182, 113358. http://dx.doi.org/10.1016/j.rser.2023.113358.

Roy, A., O'Loughlin, C.D., Chow, S.H., Randolph, M.F., 2022. Inclined loading of horizontal plate anchors in sand. Géotechnique 72 (12), 1051–1067. http://dx.doi.org/10.1680/jgeot.20.p.119.

Shan, Y., Li, X., Zhou, S., 2022. Multi-objective optimisation methodology for stiffness combination design of bridge-embankment transition zones in high-speed railways. Comput. Geotech. 145, 105242. http://dx.doi.org/10.1016/j.compgeo.2022.105242.

Sharif, Y.U., Brown, M.J., Knappett, J.A., Davidson, C., Bird, R., Coombs, W., Augarde, C., Carter, G., Macdonald, C., Johnson, K., 2025. Comparison of 1g and centrifuge modelling of drag anchors with subsurface wireless tracking. Int. J. Phys. Model. Geotech. 25 (2), 102–114. http://dx.doi.org/10.1680/jphmg.24.00029.

Shin, H.-K., Seo, B.-C., Lee, J.-H., 2011. Experimental study of embedding motion and holding power of drag embedment type anchor on hard and soft seafloor. Int. J. Nav. Archit. Ocean. Eng. 3 (3), 193–200. http://dx.doi.org/10.2478/IJNAOE-2013-0062.

Singh, V., Stanier, S., Bienen, B., Randolph, M.F., 2021. Modelling the behaviour of sensitive clays experiencing large deformations using non-local regularisation techniques. Comput. Geotech. 133, 104025. http://dx.doi.org/10.1016/j.compgeo.2021.104025.

Singh, V., Stanier, S., Bienen, B., Randolph, M.F., 2023. Calibration of strain-softening constitutive model parameters from full-field deformation measurements. Can. Geotech. J. 60 (6), 817–833. http://dx.doi.org/10.1139/cgj-2021-0342.

Thorne, C.P., 1998. Penetration and load capacity of marine drag anchors in soft clay. J. Geotech. Geoenvironmental Eng. 124 (10), http://dx.doi.org/10.1061/(ASCE)1090-0241(1998)124:10(945).

Ward Jr., J.H., 1963. Hierarchical grouping to optimize an objective function. J. Amer. Statist. Assoc. 58 (301), 236–244.

Wu, C., Zhang, Y., Wang, X., 2026. Experimental study on the effect of shank geometry, relative density and drag velocity on the installation characteristics of drag anchors in sand. Ocean Eng. 346, 123935. http://dx.doi.org/10.1016/j.oceaneng.2025.123935.

Yoon, Y.H., 2002. Prediction Methods for Capacity of Drag Anchors in Clayey Soils (Ph.D. thesis). Texas A&M University.

Zhang, Y., Fan, S., Li, S., Yin, J., 2023. Analysis of the drag anchor behaviour at shallow depths. Comput. Geotech. 160, 105518. http://dx.doi.org/10.1016/j.compgeo.2023.105518.

Zhong, Z., Zhang, S., Zhao, M., Hou, B., Gong, W., 2019. Reliability-based robust geotechnical design of spread foundations considering multiple failure modes. Comput. Geotech. 113, 103292. http://dx.doi.org/10.1016/j.compgeo.2019.103292.

Zhou, Z., O'Loughlin, C.D., White, D.J., Stanier, S.A., 2020. Improvements in plate anchor capacity due to cyclic and maintained loads combined with consolidation. Géotechnique 70 (8), 732–749. http://dx.doi.org/10.1680/jgeot.19.ti.028.

Zhou, P., Wan, S., Wang, X., Song, A., Yue, R., 2023. Topology optimization on periodic pile barriers considering material damping based on complex band diagrams. Comput. Geotech. 156, 105774. http://dx.doi.org/10.1016/j.compgeo.2023.105774.